This is the peer-reviewed, final accepted version for American Mineralogist, published by the Mineralogical Society of America.
The published version is subject to change. Cite as Authors (Year) Title. American Mineralogist, in press.
DOI: https://doi.org/10.2138/am-2023-9257. http://www.minsocam.org/

Revision 2 (word count: 4841)

Atomistic Mechanism of Al Substitution Effects on the Ferroelastic Post-stishovite Transition by High-Pressure Single-Crystal X-Ray Diffraction

Yanyao Zhang [a,b,*], Stella Chariton [c], Vitali B. Prakapenka [c], Takuo Okuchi [d], Jung-Fu Lin [a,*]

[a] Department of Earth and Planetary Sciences, Jackson School of Geosciences, The University of Texas at Austin, Austin, TX 78712, USA

[b] Present address: Earth and Planetary Sciences, Stanford University, Stanford, CA 94305, USA

[c] Center for Advanced Radiation Sources, The University of Chicago, IL 60637, USA

[d] Institute for Integrated Radiation and Nuclear Science, Kyoto University, Osaka 590-0494, Japan

[*] Corresponding authors. E-mail addresses: yanyaozh@stanford.edu (Y. Zhang), afu@jsg.utexas.edu (J.-F. Lin).

Abstract

The influence of Al substitution on the elastic properties of stishovite and its transition to post-stishovite is of great importance for interpreting the seismic wave velocities of subducted mid-ocean ridge basalt (MORB) within the mantle transition zone and the lower mantle. However, atomistic mechanisms of Al substitution effects on the transition and its associated elasticity remain debated. Here synchrotron single-crystal X-ray diffraction measurements have been performed at room temperature on Al1.3-SiO_2 (1.3 mol% Al in the chemical formula of $Si_{0.965(3)}Al_{0.041(1)}O_2H_{0.017(4)}$) and Al2.1-$SiO_2$ (2.1 mol% Al in $Si_{0.948(2)}Al_{0.064(1)}O_2H_{0.018(3)}$) crystals

This is the peer-reviewed, final accepted version for American Mineralogist, published by the Mineralogical Society of America.
The published version is subject to change. Cite as Authors (Year) Title. American Mineralogist, in press.
DOI: https://doi.org/10.2138/am-2023-9257. http://www.minsocam.org/

in diamond anvil cells with Boehler-Almax designed anvils up to 38.0 GPa and 28.5 GPa, respectively. Refinements of the diffraction patterns show that a transformation from stishovite (space group $P4_2/mnm$; No. 136) to $CaCl_2$-typed post-stishovite (space group *Pnnm*; No. 58) is accompanied by splitting of O coordinates. The Al substitution in stishovite results in a faster decrease in the O coordinate, softer apical (Si,Al)-O bonds, and a softer and less distorted $(Si,Al)O_6$ octahedron under compression. This leads to reduced adiabatic bulk modulus (K_S), shear modulus (G), shear wave velocity (V_S), and compressional wave velocity (V_P) in the stishovite phase, explaining seismic wave perturbations in the mantle transition zone. Together with Raman data, Landau theory modeling shows that Al substitution increases the order parameter and excess free energy, stabilizing the post-stishovite phase at lower pressures. Correlation between elasticity and octahedral distortion index (D) reveals that at certain D, the Al substitution reduces K_S, G, V_S, and V_P of the stishovite phase while increasing G, V_S, and V_P of the post-stishovite phase. Importantly, the maximum shear reduction is slightly enhanced at D = 0.00620(9) at the transition point. Our results help explain the seismically observed small-scale V_S anomalies beneath subduction regions in the shallow lower mantle where Al,H-bearing stishovite undergoes the post-stishovite transition.

Keywords: Al,H-bearing stishovite, single-crystal X-ray diffraction, ferroelastic transition, post-stishovite, lower-mantle seismic scatterers, elasticity

Running title (60 characters with spaces): Atomic Mechanism of Al,H-Bearing Post-Stishovite Transition

This is the peer-reviewed, final accepted version for American Mineralogist, published by the Mineralogical Society of America.
The published version is subject to change. Cite as Authors (Year) Title. American Mineralogist, in press.
DOI: https://doi.org/10.2138/am-2023-9257. http://www.minsocam.org/

Introduction

Stishovite is expected to be an abundant component in subducted mid-ocean ridge basalt (MORB) in the mantle transition zone and the lower mantle (Hirose et al. 1999; Litasov and Ohtani 2005; Ishii et al. 2019). Previous experimental studies have shown that in a MORB composition, stishovite can accommodate up to 10.2 wt% Al_2O_3, together with a certain amount of hydrogen, in its structure mainly through charge-coupled substitutions of $Al^{3+} + H^{+} = Si^{4+}$ and $2Al^{3+} + OV^{2+}$ (oxygen vacancy) $= 2Si^{4+}$ (Tsutsumi et al. 2024). The Al substitution can affect the elastic properties of stishovite and post-stishovite transition as well as the transition depth, which are of great importance in understanding seismic wave properties of subducting MORB in the deep Earth. Specifically, previous X-ray diffraction studies have shown that 1.82-5.37 wt% Al_2O_3 substitution can reduce the density of stishovite by ~0.2-1.2% at 15 GPa (Ono et al. 2002; Lakshtanov et al. 2005; Zhang et al. 2022; Criniti et al. 2023). Previous ultrasonic data have shown that 3.43 wt% Al_2O_3 substitution reduces the shear wave velocity (V_S) and compressional wave velocity (V_P) of stishovite by ~4.1% and ~3.5%, respectively, at 18.4 GPa and 1700 K (Gréaux et al. 2016). These findings have been used to interpret the negative sound velocity perturbation in the mantle transition zone (Simmons and Gurrola 2000; Tauzin et al. 2013; Gréaux et al. 2016).

Of particular interest in deep-mantle seismology is the role of Al dissolution on the depths of the post-stishovite transition and its associated velocity reductions (Lakshtanov et al. 2005, 2007b; Bolfan-Casanova et al. 2009; Umemoto et al. 2016; Zhang et al. 2022; Criniti et al. 2023),

because this can be associated with the observed small-scale negative V_S anomalies beneath subduction region in the shallow lower mantle (Niu et al. 2003; Kaneshima 2016, 2019; Zhang et al. 2022). The Al substitution in stishovite can significantly lower the transition pressure: 3.43-6.07 wt% Al_2O_3 substitution in stishovite can reduce the transition pressure from ~52 GPa to 16-24 GPa (Andrault et al. 1998; Lakshtanov et al. 2007b; Bolfan-Casanova et al. 2009; Zhang et al. 2022). Previous Landau modeling based on the pseudo-proper typed ferroelastic transition mechanism shows that the Al substitution reduces elastic coefficients C_{11}, C_{33}, C_{44}, and C_{66}, has negligible effects on C_{13}, and increases C_{12} (Zhang et al. 2022). The reduced C_{11} and increased C_{12} lead to the two moduli equal to each other at a lower pressure, causing the shear instability (Zhang et al. 2022). Additionally, the Al substitution reduces adiabatic bulk modulus (K_S), shear modulus (G), V_S, and V_P of the stishovite phase but it enhances those elastic properties of the post-stishovite phase (Zhang et al. 2022). Importantly, 3.43-5.37 wt% Al_2O_3 substitution can cause a maximum V_S reduction of ~29% across the transition, slightly larger than ~26% V_S reduction in pure-endmember stishovite (Zhang et al. 2021, 2022).

To better understand the effects of the Al substitution on the phase transition and elasticity, high-quality single-crystal structural data are needed to decipher the atomistic evolution across the post-stishovite transition. Previous single-crystal X-ray diffraction (SCXRD) experiments on Al0.6-SiO_2 and Al1.7-SiO_2 crystals at ambient conditions have shown that Al substitution induces minimal changes in atomic positions and slight alterations in bond lengths and bond angles (Smyth et al. 1995; Criniti et al. 2023). Although high-pressure SCXRD data were collected on the Al1.7-SiO_2 crystal in Criniti et al. (2023), the effect of Al substitution on atomistic parameters (such as oxygen coordinate, bond length, and bond angle) and polyhedral

parameters (such as octahedral volume, distortion, and rotation) was not fully discussed. Importantly, the effects of the atomistic parameters on the elasticity across the transition that is needed for deep-mantle geophysical applications largely remain unclear.

In light of this, we have conducted synchrotron SCXRD experiments on Al1.3-SiO_2 and Al2.1-SiO_2 crystals up to 38.0 GPa and 28.5 GPa, respectively, using Boehler-Almax designed anvils in diamond anvil cells (DACs). These data are refined to reveal the Al effects on atomistic and $(Si,Al)O_6$ octahedral parameters. The results are used with Raman data and Landau theory modeling to understand the effect of Al substitution on the sound velocities and elastic moduli across the post-stishovite transition in the deep mantle.

Experimental details

Al-bearing stishovite crystals were synthesized using both 5000-ton and 1000-ton Kawai-type multi-anvil apparatus with run# 5K3302 and 1K2965, respectively, at the Institute for Planetary Materials at Okayama University. Details of sample synthesis and characterization can be found in Zhang et al. (2022). Briefly, run# 5K3302 was synthesized at 20 GPa and 1973 K for 16.5 hours while run# 1K2965 was synthesized at 19.2 GPa and 1973 K for 7 hours. Qualitative chemical mappings on selected large crystals using a scanning electron microscopy with energy dispersive X-ray spectroscopy (SEM/EDS) have shown that Si, Al, and O elements distribute homogeneously throughout the crystals. Further quantitative chemical analysis using a JEOL Electron Microprobe (EPMA) has shown that the crystals contain 95.86(101) wt% SiO_2 and 3.43(6) wt% Al_2O_3 in run# 5K3302 and 94.20(49) wt% SiO_2 and 5.37(4) wt% Al_2O_3 in run#

111 1K2965 (Zhang et al. 2022). Unpolarized Fourier-transform infrared spectroscopy (FTIR)
112 measurements were conducted on crystals with an orientation close to the *ac* plane. Water
113 contents of the crystals were estimated to be 0.2497(500) wt% H_2O in run# 5K3302 and
114 0.2678(500) wt% H_2O in run# 1K2965 (Zhang et al. 2022). The uncertainties were estimated
115 from the background subtraction, peak deconvolution, and sample thickness measurements.
116 These uncertainties are consistent with uncertainties in previous works (Litasov et al. 2007; Ishii
117 et al. 2022). We should note that unpolarized FTIR measurements on different orientations can
118 result in different water contents because the O-H absorption is strongly anisotropic between *a*-
119 axis and *c*-axis in stishovite at ambient conditions (Litasov et al. 2007; Ishii et al. 2022).
120 Analyses of EPMA and FTIR results show the chemical formula of $Si_{0.965(3)}Al_{0.041(1)}O_2H_{0.017(4)}$
121 and $Si_{0.948(2)}Al_{0.064(1)}O_2H_{0.018(3)}$ for the crystals in run# 5K3302 and run# 1K2965, respectively
122 (Table S1). Using the Al content in mol% in the chemical formula, we denoted the crystals in
123 run# 3305 as Al1.3-SiO_2 and those in run# 1K2965 as Al2.1-SiO_2. Analysis of synchrotron
124 SCXRD data at ambient conditions shows a tetragonal structure with the $P4_2/mnm$ space group
125 (No. 136) for these crystals.

126

127 Short-symmetric DACs equipped with diamond anvils with Boehler-Almax design and 300 μm
128 culets and tungsten-carbide seats with a large aperture of ~80° (4θ) were used in the high-
129 pressure SCXRD measurements. A piece of 260 μm thick rhenium gasket was pre-indented to
130 ~35 μm thick, and a hole with a diameter of 190 μm was drilled in the center of the pre-indented
131 area to serve as a sample chamber. We double-side polished Al1.3-SiO_2 and Al2.1-SiO_2 crystals
132 down to 10-15 μm using 3M diamond films and then cut them to approximately 20 by 30 μm big
133 using a razor blade. These two batches of crystals were loaded into the sample chamber of a

DAC separately, together with platinum (Pt) and ruby as pressure calibrants. Ruby was used to determine pressure after gas loading while Pt was used to measure pressure during in situ SCXRD measurements. Neon was finally loaded into the chamber up to 0.14479 GPa as a pressure medium in the Mineral Physics Laboratory at the University of Texas at Austin. The pressure after neon loading was measured by shifts of the fluorescence peak of ruby (Dewaele et al. 2008).

High-pressure synchrotron SCXRD experiments were performed on the Al1.3-SiO_2 and Al2.1-SiO_2 crystals at the beamline 13ID-D of the GSECARS, Advanced Photon Source, Argonne National Laboratory. An incident X-ray beam with 0.2952 Å wavelength and 10% intensity was focused on 3 by 3 μm^2 areas of each crystal. The sample stage was rotated over ±33° about its vertical axis. XRD frames were collected 1 or 2 s at every 0.5° of the rotation by a CdTe Pilatus 1 M detector. The total number of frames is 132 for each crystal. A membrane setup was used to control pressure in DAC which was determined by the unit-cell volume of Pt based on its equation of state (EoS) parameters (Fei et al. 2007). The SCXRD data were collected every 2-3 GPa up to 38.0 GPa for the Al1.3-SiO_2 crystal and up to 28.5 GPa for the Al2.1-SiO_2 crystal. Together with the use of the Boehler-Almax anvils with an opening (4θ) of ~80°, the experimental setup allowed us to obtain more reflection spots especially with small *d*-spacings and to avoid intensity saturations of the spots.

We followed the same procedure as Zhang et al. (2023) to resolve and refine crystal structures. To begin with, CrysAlisPRO was used to find a proper unit cell, calculate unit-cell parameters,

determine intensity for each *hkl* reflection, and then correct for absorption using the SCALE3 ABSPACK scaling algorithm for the crystal (Rigaku 2015). We inspected the R_{int} value to evaluate the quality of the intensity integration and selected datasets with $R_{int} < 14\%$ before proceeding with the structural refinements in the JANA software (Petrícek et al. 2014). The space group and crystal structure of the samples were determined using a charge-flipping algorithm (Petrícek et al. 2014). Site occupancies of Si and Al were fixed to be 0.960 Si and 0.040 Al for the Al1.3-SiO_2 crystal and 0.937 Si and 0.063 Al for the Al2.1-SiO_2 crystal based on the EPMA analysis results (Zhang et al. 2022). The H atom was not included in the structural refinement due to its low concentration and small atomic scattering factor (i.e., low diffracting power). Eventually, the atomic coordinates and isotropic/anisotropic displacement parameters were refined, and the quality of the structural refinements was evaluated by the residual R_1 factor. Bond lengths, bond angles, and polyhedral parameters were calculated with the VESTA software (Table 1) (Momma and Izumi 2011). The Crystallographic Information Files (CIF) for both Al1.3-SiO_2 and Al2.1-SiO_2 crystals at different pressures can be found in supplementary materials.

Results and Discussion

Unit-cell parameters and space groups

Analysis of unwarped images of the *hk*1 and *hk*2 reciprocal planes shows the splitting of the reflection spots at high pressure in both Al1.3-SiO_2 and Al2.1-SiO_2 crystals (Fig. 1). This twinning has been reported in Al-stishovite upon transformation to post-stishovite in previous studies (Lakshtanov et al. 2007b; Criniti et al. 2023), and is indicative of a ferroelastic transition

178 (Salje 1993). To evaluate the crystal quality under pressure, we integrated the 110 peak in both
179 azimuthal angle (χ) and diffraction angle (2θ) at low pressure and peak pressure, and then
180 calculated the full-width at half maximum (FWHM). The FWHM values in χ are 1.34° at 5.8
181 GPa and 1.16° at 38.0 GPa for the Al1.3-SiO_2 crystal, and 1.11° at 6.5 GPa and 1.20° at 28.5
182 GPa for the Al2.1-SiO_2 crystal, showing no significant change with pressure (Fig. 1). FWHM in
183 2θ also shows similar values at low and peak pressures in both crystals. These results along with
184 other confidence factors, such as the R_{int} and R_1 values (shown later), indicate the preservation of
185 crystal quality and thus, the validity of our refinements at high pressure.

186

187 The R_{int} values range from 1.27% to 13.69% for Al1.3-SiO_2, and from 0.67% to 2.13% for Al2.1-
188 SiO_2. Analysis of lattice parameters at high pressure shows that *a* axis splits into *a* and *b* axis at
189 ~16.1 GPa in Al1.3-SiO_2 and ~21.1 GPa in Al2.1-SiO_2, while the length of *c* axis and unit-cell
190 volume decrease continuously throughout the compression (Fig. S1). For the Al1.3-SiO_2
191 stishovite phase, a weighted 3rd-order Birch-Murnaghan (BM) EoS fit with EosFit-GUI
192 (Gonzalez-Platas et al. 2016) up to 21.0 GPa gives an ambient isothermal bulk modulus (K_{T0}) of
193 285.8(41) GPa and a first-order pressure derivative (K_{T0}') of 3.8(6) with a fixed ambient volume
194 (V_0) of 47.079 Å^3 (Angel 2000) (Fig. S2; Table S2). Since K_{T0}' is refined to 4 within the
195 uncertainties, it should be fixed at 4 in the 2nd-order BM EoS fit, yielding K_{T0} = 284.8(15) GPa.
196 Similarly, the weighted 3rd-order BM EoS fit to the Al2.1-SiO_2 stishovite data up to 14.6 GPa
197 gives K_{T0} = 289.0(224) GPa and K_{T0}' = 5.9(46) with a fixed V_0 of 47.389 Å^3 (Gonzalez-Platas et
198 al. 2016). With K_{T0}' fixed at 4, the 2nd-order BM EoS fit yields K_{T0} = 298.2(70) GPa.

199

To further determine the crystal's space group, a subset of collected reflections was selected, where the intensity (I) exceeds three times the standard deviation (σ) of the intensity (i.e., $I > 3\sigma(I)$). The Al1.3-SiO_2 and Al2.1-SiO_2 crystals maintain a tetragonal structure with the $P4_2/mnm$ space group (No. 136) up to 21.0 and 14.6 GPa, respectively (Fig. 2). They further adopt an orthorhombic structure with the *Pnnm* space group (No. 58) above 26.3 and 22.0 GPa, respectively (Fig. 2). This is consistent with previous Raman and XRD analyses, which show that the post-stishovite transition occurs at 21.1(6) GPa in the Al1.3-SiO_2 crystal and 16.1(4) GPa in the Al2.1-SiO_2 crystal (Zhang et al. 2022). The decrease of the transition pressure in stishovite can be attributed to the Al and H substitution, hydration, or the presence of deviatoric stress during compression (Lakshtanov et al. 2007b; Nisr et al. 2017; Wang et al. 2023). A recent DAC study, conducted without a pressure medium, shows that a deviatoric stress of ~2.5 GPa shifts the transition from 51(2) to 14.9(3) GPa in pure-endmember stishovite (Wang et al. 2023). Our high-pressure experiments under quasi-hydrostatic conditions exhibit a small deviatoric stress of less than 0.5 GPa (Wang et al. 2023), which would have a minimal effect on the transition pressure as compared to the Al and H substitution.

Atomistic parameters

The refined symmetries of both stishovite and post-stishovite phases suggest that the Si or Al atoms are located at (0, 0, 0) and the O atoms are located at (Ox, Oy, 0). The coordinates Ox and Oy, together with isotropic/anisotropic displacement parameters of all atoms, were further refined until R_1 reached the minimum. The final R_1 values range from 2.89% to 6.65% for Al1.3-SiO_2 and from 5.08% to 6.34% for Al2.1-SiO_2.

222

223 Analysis of refined oxygen coordinates shows that Ox(y) in the stishovite structure decreases
224 monotonically from 0.3061(3) at ambient pressure to 0.3043(4) at 21.0 GPa for Al1.3-SiO_2 and
225 from 0.3062(5) at ambient pressure to 0.3043(4) at 14.6 GPa for Al2.1-SiO_2 (Fig. 3a). Together
226 with previously reported data on stishovite with different Al contents (Smyth et al. 1995; Criniti
227 et al. 2023; Zhang et al. 2023), the Al substitution has negligible effects on the ambient Ox(y)
228 (Fig 4a). Additionally, the Al substitution decreases the slope at high pressure when considering
229 data for pure stishovite from Zhang et al. (2023) and Al-bearing stishovite data from our study
230 (Fig. 4b). Across into the post-stishovite phase, the oxygen coordinate splits into Ox and Oy,
231 indicating a symmetry breaking from tetragonal to orthorhombic structure (Andrault et al. 1998)
232 (Fig. 3a).

233

234 The apical (Si,Al)-O3 and equatorial (Si,Al)-O1(2) bond lengths of both samples decrease with
235 increasing pressure (Fig. 3b). We fitted the Al1.3-SiO_2 stishovite's data up to 21.0 GPa using the
236 2nd-order linear BM EoS (Angel 2000) in EosFit-GUI (Gonzalez-Platas et al. 2016), giving linear
237 modulus $K_{0,(Si,Al)-O3}$ = 556(9) GPa and $K_{0,(Si,Al)-O1(2)}$ = 1287(35) GPa (Table 2). Similarly, the
238 EoS fit to the Al2.1-SiO_2 stishovite's data up to 14.6 GPa yields $K_{0,(Si,Al)-O3}$ = 478(13) GPa and
239 $K_{0,(Si,Al)-O1(2)}$ = 1807(121) GPa (Table 2). The Al substitution can increase both bond lengths at
240 ambient conditions because Al^{3+} has larger effective ionic radius than Si^{4+} (0.535 Å vs. 0.400 Å)
241 (Shannon et al. 1976) (Fig. 4c). The 5.37 wt% Al_2O_3 substitution (0.064 Al atoms per formula
242 unit (apfu)) can make the apical (Si,Al)-O3 bond ~22.7% more compressible whereas the

equatorial (Si,Al)-O1(2) bond ~24.4% less compressible compared to pure-endmember stishovite (Zhang et al. 2023) (Fig. 4d).

The bond angles change little (< 1%) at high pressure (Fig. 3c), similar to the behavior in pure endmember stishovite and post-stishovite (Zhang et al. 2023). This indicates a negligible Al substitution effect on the band angles.

(Si,Al)O_6 octahedron

The volume of the (Si,Al)O_6 octahedron decreases continuously throughout the entire compression range in both Al1.3-SiO_2 and Al2.1-SiO_2 crystals (Fig. 5a; Table 1). A fit of the octahedral volumes with the 2nd-order BM EoS yields the parameter $K_{0,oct}$ = 304.6(26) GPa for the Al1.3-SiO_2 stishovite and $K_{0,oct}$ = 333.1(83) GPa for the Al2.1-SiO_2 stishovite (Angel 2000; Gonzalez-Platas et al. 2016) (Table 2). A comparison between the linear moduli $K_{0,(Si,Al)-O3}$ and $K_{0,(Si,Al)-O1(2)}$ shows that the stiffness of the (Si,Al)O_6 octahedron is mainly contributed by four equatorial (Si,Al)-O1(2) bonds, which are 2.3 to 3.8 times stiffer than the two apical bonds. The octahedra are stacked along the *c*-axis by sharing two equatorial edges, while they only share vertices perpendicular to the *c*-axis (Fig. 2). Therefore, interatomic repulsion is much stronger in the equatorial plane (parallel to the *c*-axis), which correlates well with the *c*-axis being much less compressible than the *a*-axis. Furthermore, a comparison between $K_{0,oct}$ and K_{T0} shows that the (Si,Al)O_6 octahedron is stiffer than the unit cell. The stishovite's unit cell also includes interstitial spaces between octahedra which can undergo polyhedral distortion and relative displacement. These can result in the lower bulk modulus of the unit cell compared to the

individual octahedra (Figs. 5b and 5c). On the other hand, the Al substitution increases the ambient volume of the octahedron and enhances its compressibility at high pressure in the stishovite phase, which is consistent with previous studies (Smyth et al. 1995; Criniti et al. 2023; Zhang et al. 2023) (Figs. 6a and 6b).

The distortion of the $(Si,Al)O_6$ octahedron can be evaluated by distortion index (D) and bond angle variance (σ^2), which describe the deviation from an ideal octahedral geometry with respect to its bond length and bond angle, respectively. D can be calculated by a formula of $D(\%) = \frac{100}{6}\sum_{i=1}^{6}\left|l_i - l_{avg}\right|/l_{avg}$, where l_i is the i^{th} (Si,Al)-O bond length in an octahedron and l_{avg} is the average of six mean (Si,Al)-O bond length in an octahedron (Renner and Lehmann 1986). D decreases with increasing pressure, indicating that the octahedron becomes less distorted under compression in both stishovite and post-stishovite phases (Fig. 5b; Table 1). Compared to the pure SiO_6 octahedron (Zhang et al. 2023), the $(Si,Al)O_6$ octahedron is slightly more distorted at ambient conditions but becomes less distorted under compression (Figs. 6c and 6d). This effect also aligns with previously reported data (Smyth et al. 1995; Criniti et al. 2023; Zhang et al. 2023) (Figs. 6c and 6d). On the other hand, σ^2 can be calculated by $\sigma^2(deg^2) = \frac{1}{11}\sum_{i=1}^{12}(\alpha_i - 90°)^2$, where α_i is the i^{th} ∠O-(Si,Al)-O in an octahedron (Robinson et al. 1971). In the stishovite phase region, σ^2 remains almost unchanged under pressure for the Al1.3-SiO_2 crystal, while decreases with increasing pressure for the Al2.1-SiO_2 crystal (Fig 5c; Table 1). Crossing into the post-stishovite region, σ^2 increases for both crystals (Fig 5c; Table 1). The Al substitution slightly decreases the angle distortion at ambient conditions, while making the octahedron less distorted in Al2.1-SiO_2 (Figs 6e and 6f).

This is the peer-reviewed, final accepted version for American Mineralogist, published by the Mineralogical Society of America.
The published version is subject to change. Cite as Authors (Year) Title. American Mineralogist, in press.
DOI: https://doi.org/10.2138/am-2023-9257. http://www.minsocam.org/

As the tetragonal symmetry breaks down into the orthorhombic symmetry, the $(Si,Al)O_6$ octahedron rotates about the *c* axis in the post-stishovite phase. The rotation angle, Φ, can be calculated using lattice parameters, a_{Pst} and b_{Pst}, and oxygen coordinates in the formula of $\Phi(°) = 45° - \arctan(a_{Pst} \cdot 0x/b_{Pst}/0y)$ (Range et al. 1987; Zhang et al. 2023). Φ increases nonlinearly from 0° in the stishovite phase up to 2.2° at 38.0 GPa in the Al1.3-SiO_2 post-stishovite and 2.1° at 28.5 GPa in the Al2.1-SiO_2 post-stishovite phase (Fig. S3; Table 1). This nonlinear increase under pressure results in a nonlinear pressure dependence of the Raman shift of the A_g mode which represents a rotational vibration of O in the $(Si,Al)O_6$ octahedron about the *c* axis (Hemley et al. 1986).

Hydrogen substitution effects on the transition pressure

In the absence of hydrogen, Al substitution into stishovite has been proposed to occur through the coupled Al^{3+} and OV^{2+} substitution (SiO_2-$AlO_{1.5}$) (Pawley et al. 1993; Litasov et al. 2007). Previous DAC experiments have shown that dry stishovite with ~3.1 wt% Al_2O_3 undergoes the post-stishovite at ~21.5(15) GPa and 300 K (Bolfan-Casanova et al. 2009). Furthermore, hydrogen can be incorporated into stishovite's structure mainly through direct hydrogen or water molecule substitution (SiO_2-H_2O) (Spektor et al. 2011; Lin et al. 2022; Li et al. 2023) and coupled Al^{3+} and H^+ substitution with Si^{4+} (SiO_2-AlOOH) (Pawley et al. 1993; Litasov et al. 2007). Al-free stishovite with 3.2(5) wt% H_2O transforms to the post-stishovite phase at 28-42 GPa and 300 K (Nisr et al. 2017), while stishovite with an Al/H ratio close to unity undergoes the transition at 0 GPa and 300 K (Ishii et al. 2022).

We further also evaluate how the total Al and H content can affect the transition pressure. Comparison between the transition pressure and (Al+H)/Si ratio data shows two separate trends which can be classified by the SiO_2-H_2O and SiO_2-AlOOH-$AlO_{1.5}$ substitutions (Fig. 7b). Linear fits with fixed transition pressure of pure-endmember stishovite at 53.2 GPa show a reduction rate of -82.5(2) GPa for the SiO_2-H_2O substitution and -460(45) GPa for the SiO_2-AlOOH-$AlO_{1.5}$ substitution. This indicates that Al (and H) substitution has more significant effects on the transition pressure reduction than the H substitution alone.

Implications

Atomistic understanding of Al effects on post-stishovite transition

The atomistic parameters of the study are used with a pseudo-proper typed Landau model (Carpenter et al. 2000) and Raman data to provide new insights into Al effects on the post-stishovite transition and the associated elasticity. The symmetry-breaking spontaneous strain, e_1-e_2, is calculated using a formula of $e_1 - e_2 = (a_{Pst} - b_{Pst})/\sqrt{a_{Pst} \times b_{Pst}}$ (Carpenter et al. 2000). The modeled results show that e_1-e_2 decreases linearly with the octahedral rotation angle, Φ, and this linear trend in Al-bearing crystals from our study and Criniti et al. (2023) is very similar to that in the pure-endmember SiO_2 (Zhang et al. 2023) (Fig. 8a). This indicates that the Al substitution has negligible effects on the symmetry-breaking strain at certain degree of the (Si,Al)O_6 octahedron rotation. On the other hand, the free energy difference between post-stishovite and stishovite is a polynomial expression of the order parameter, Q, which describes the driving force of the transition (Carpenter et al. 2000). A previous SCXRD study on pure-

endmember post-stishovite has revealed that Q increases linearly with Φ (Zhang et al. 2023). A comparison of linear Q-Φ relationships between our Al-bearing and previous pure-endmember crystals (Zhang et al. 2023) shows that the Al substitution can increase the slope of the relation (Fig. 8b). That is, at a given Φ, Q is larger, and thus, the free energy difference between post-stishovite and stishovite becomes larger in the Al-bearing crystals (Fig. 8c). Therefore, the Al substitution can stabilize the post-stishovite phase at a relatively lower pressure than the pure-endmember counterpart.

Atomistic mechanisms of deep-mantle elasticity

Previous studies have shown that the Al substitution in the stishovite phase can reduce its density at ambient conditions (Smyth et al. 1995; Ono et al. 2002; Lakshtanov et al. 2007a; Litasov et al. 2007; Zhang et al. 2021, 2022; Criniti et al. 2023). This can be explained by increased apical and equatorial (Si,Al)-O bond lengths and increased V_{oct} at ambient conditions (Figs. 4c and 6a). Moreover, the 4.36 wt% Al_2O_3 substitution can reduce the ambient bulk and shear modulus by 6.3 or 12.6% and 3.2 or 14.9%, respectively, based on previous Brillouin or ultrasonic studies (Lakshtanov et al. 2007a; Gréaux et al. 2016). The reduction in the bulk modulus is caused by the decrease in the octahedral bulk modulus $K_{0,oct}$ and linear modulus $K_{0,(Si,Al)-O3}$ (Figs. 4d and 6b). Zhang et al. (2023) showed that shear modulus along [110] direction, (C_{11}-C_{12})/2, decreases as the distortion index D decreases. If this correlation also applies to Al-bearing stishovite, then the rapid decrease of D would be predicted to result in a reduced shear modulus at given pressure in Al-bearing stishovite.

353 We further co-plot C_{ij}, K_S, G, V_P, and V_S as a function of D to evaluate how the elasticity changes
354 with octahedral distortion (Fig. 9). The C_{ij}, K_S, G, V_P, and V_S values of the Al1.3-SiO_2 and Al2.1-
355 SiO_2 crystals at high pressures were taken from previous Landau modeling results (Carpenter et
356 al. 2000; Zhang et al. 2022). All C_{ij}'s of Al-bearing stishovite increase with decreasing D, except
357 for C_{11} which shows a slight decrease (Figs. 9a and 9b). The decreased C_{11} and increased C_{12}
358 converge at D = 0.00611-0.00628, contrasting with pure-endmember stishovite where the two
359 moduli converge at nearly zero D (Andrault et al. 1998; Zhang et al. 2023). At certain D, Al-
360 bearing stishovite shows significantly lower shear moduli, C_{44} and C_{66} , than pure-endmember
361 stishovite (Zhang et al. 2023) (Fig. 9b). This Al effect results from the decreased oxygen
362 coordinate *Ox(y)* and octahedral angle variance σ^2 at high pressure that can make the shear
363 deformation along the principal planes (i.e., the (100), (010), (001) planes) easier. In the post-
364 stishovite region, Al2.1-SiO_2 shows steeper C_{33} and C_{66} and slightly larger splitting of C_{11}, C_{13},
365 and C_{44} than Al1.3-SiO_2 (Figs. 9a and 9b). This contributes to the stability of the post-stishovite
366 structure at lower pressures when Al substitutes. Furthermore, Al-bearing stishovite shows lower
367 K_S, G, V_P, and V_S compared to pure-endmember stishovite at certain D values. When comparing
368 Al1.3-SiO_2 and Al2.1-SiO_2, the Al substitution enhances the maximum reductions of G, V_P, and
369 V_S at D = 0.00611-0.00628, where the transition occurs, and also these elastic properties of the
370 post-stishovite phase (Figs. 9c and 9d).

371

372 Our SCXRD data have revealed the role of Al substitution in the post-stishovite transition and its
373 associated elastic properties, and thus, can provide new insights into geophysical behavior of the
374 post-stishovite transition in subducted mid-ocean ridge basalt (MORB) within the mantle
375 transition zone and the shallow lower mantle. The decrease in K_S and G with the Al substitution

in stishovite could be due to smaller O coordinates, softer (Si,Al)-O3 bonds, and less distorted (Si,Al)O_6 octahedra. At a given degree of the (Si,Al)O_6 octahedra distortion, the Al substitution leads to smaller K_S, G, V_P, and V_S values in the stishovite phase. This reduction in sound velocities can be used to explain -3.4% V_P and -4.2% V_S perturbations in the mantle transition zone (Simmons and Gurrola 2000; Tauzin et al. 2013; Gréaux et al. 2016). On the other hand, the Al substitution enhances Q and excess free energy at certain degree of the octahedral rotation, and thus, can stabilize the post-stishovite phase at lower pressures compared to pure-endmember stishovite. At certain degree of octahedral distortion, the Al substitution reduces elastic moduli and sound velocities of stishovite and slightly enhances maximum shear reduction at D = 0.00611-0.00628. This Al-dependent transition pressure and associated elasticity can be used to help explain the seismically-observed small-scale V_S anomalies beneath subduction regions in the shallow lower mantle (Niu et al. 2003; Lakshtanov et al. 2007b; Kaneshima 2016, 2019; Zhang et al. 2022).

Acknowledgments and Funding

High-pressure SCXRD experiments were performed at 13ID-D, GSECARS, which was supported by the National Science Foundation (EAR-0622171). This research used resources of the Advanced Photon Source, a U.S. Department of Energy (DOE) Office of Science User Facility operated for the DOE Office of Science by Argonne National Laboratory under Contract No. DE-AC02-06CH11357. Jung-Fu Lin acknowledges support from Geophysics Program of the U.S. National Science Foundation (EAR-2001381 and EAR-2333879). The authors also acknowledge support from the Joint-Use User Program of the Institute for Planetary Materials, Okayama University. Takuo Okuchi was supported by JSPS KAKENHI Grant Number

399 21H04519 and the Joint-Use User Program of the Institute for Integrated Radiation and Nuclear
400 Science, Kyoto University.

401

402 **References Cited**

403 Andrault, D., Fiquet, G., Guyot, F., and Hanfland, M. (1998) Pressure-induced Landau-type
404 transition in stishovite. Science, 282, 720–724.

405 Angel, R.J. (2000) Equations of State. Reviews in Mineralogy and Geochemistry, 41, 35–59.

406 Bolfan-Casanova, N., Andrault, D., Amiguet, E., and Guignot, N. (2009) Equation of state and
407 post-stishovite transformation of Al-bearing silica up to 100 GPa and 3000 K. Physics of
408 the Earth and Planetary Interiors, 174, 70–77.

409 Carpenter, M.A., Hemley, R.J., and Mao, H. (2000) High-pressure elasticity of stishovite and the
410 P42/mnm = Pnnm phase transition. Journal of Geophysical Research: Solid Earth, 105,
411 807–816.

412 Criniti, G., Ishii, T., Kurnosov, A., Glazyrin, K., and Ballaran, T.B. (2023) High-pressure phase
413 transition and equation of state of hydrous Al-bearing silica. American Mineralogist, in
414 press.

415 Dewaele, A., Torrent, M., Loubeyre, P., and Mezouar, M. (2008) Compression curves of
416 transition metals in the Mbar range: Experiments and projector augmented-wave
417 calculations. Physical Review B - Condensed Matter and Materials Physics, 78, 1–13.

418 Fei, Y., Ricolleau, A., Frank, M., Mibe, K., Shen, G., and Prakapenka, V. (2007) Toward an
419 internally consistent pressure scale. Proceedings of the National Academy of Sciences of

420 the United States of America, 104, 9182–9186.

421 Gonzalez-Platas, J., Alvaro, M., Nestola, F., and Angel, R. (2016) EosFit7-GUI: a new graphical
422 user interface for equation of state calculations, analyses and teaching. Journal of Applied
423 Crystallography, 49, 1377–1382.

424 Gréaux, S., Kono, Y., Wang, Y., Yamada, A., Zhou, C., Jing, Z., Inoue, T., Higo, Y., Irifune, T.,
425 Sakamoto, N., and others (2016) Sound velocities of aluminum-bearing stishovite in the
426 mantle transition zone. Geophysical Research Letters, 43, 4239–4246.

427 Hemley, R.J., Mao, H.-K., and Chao, E.C.T. (1986) Raman Spectrum of Natural and Synthetic
428 Stishovite. Physics and Chemistry of Minerals, 13, 285–290.

429 Hirose, K., Fei, Y., Ma, Y., and Mao, H.K. (1999) The fate of subducted basaltic crust in the
430 Earth's lower mantle. Nature, 397, 53–56.

431 Ishii, T., Kojitani, H., and Akaogi, M. (2019) Phase Relations of Harzburgite and MORB up to
432 the Uppermost Lower Mantle Conditions: Precise Comparison With Pyrolite by
433 Multisample Cell High-Pressure Experiments With Implication to Dynamics of Subducted
434 Slabs. Journal of Geophysical Research: Solid Earth, 124, 3491–3507.

435 Ishii, T., Criniti, G., Ohtani, E., Purevjav, N., Fei, H., Katsura, T., and Mao, H.K. (2022)
436 Superhydrous aluminous silica phases as major water hosts in high-temperature lower
437 mantle. Proceedings of the National Academy of Sciences of the United States of America,
438 119, 1–6.

439 Kaneshima, S. (2016) Seismic scatterers in the mid-lower mantle. Physics of the Earth and
440 Planetary Interiors, 257, 105–114.

——— (2019) Seismic scatterers in the lower mantle near subduction zones. Geophysical Journal International, 218, 1873–1891.

Lakshtanov, D.L., Vanpeteghem, C.B., Jackson, J.M., Bass, J.D., Shen, G., Prakapenka, V.B., Litasov, K., and Ohtani, E. (2005) The equation of state of Al,H-bearing SiO 2 stishovite to 58 GPa. Physics and Chemistry of Minerals, 32, 466–470.

Lakshtanov, D.L., Litasov, K.D., Sinogeikin, S. V., Hellwig, H., Li, J., Ohtani, E., and Bass, J.D. (2007a) Effect of Al3+ and H+ on the elastic properties of stishovite. American Mineralogist, 92, 1026–1030.

Lakshtanov, D.L., Sinogeikin, S. V., Litasov, K.D., Prakapenka, V.B., Hellwig, H., Wang, J., Sanches-Valle, C., Perrillat, J.P., Chen, B., Somayazulu, M., and others (2007b) The post-stishovite phase transition in hydrous alumina-bearing SiO 2 in the lower mantle of the earth. Proceedings of the National Academy of Sciences of the United States of America, 104, 13588–13590.

Li, J., Lin, Y., Meier, T., Liu, Z., Yang, W., Mao, H.K., Zhu, S., and Hu, Q. (2023) Silica-water superstructure and one-dimensional superionic conduit in Earth's mantle. Science Advances, 9.

Lin, Y., Hu, Q., Yang, J., Meng, Y., Zhuang, Y., and Mao, H.-K. (2022) Hydrous SiO2 in subducted oceanic crust and water transport to the core-mantle boundary. Earth and Planetary Science Letters, 594, 117708.

Litasov, K.D., and Ohtani, E. (2005) Phase relations in hydrous MORB at 18-28 GPa: Implications for heterogeneity of the lower mantle. Physics of the Earth and Planetary Interiors, 150, 239–263.

463 Litasov, K.D., Kagi, H., Shatskiy, A., Ohtani, E., Lakshtanov, D.L., Bass, J.D., and Ito, E. (2007)
464 High hydrogen solubility in Al-rich stishovite and water transport in the lower mantle. Earth
465 and Planetary Science Letters, 262, 620–634.

466 Momma, K., and Izumi, F. (2011) VESTA 3 for three-dimensional visualization of crystal,
467 volumetric and morphology data. Journal of Applied Crystallography, 44, 1272–1276.

468 Nisr, C., Leinenweber, K., Prakapenka, V., Prescher, C., Tkachev, S., and Shim, S.H.D. (2017)
469 Phase transition and equation of state of dense hydrous silica up to 63 GPa. Journal of
470 Geophysical Research: Solid Earth, 122, 6972–6983.

471 Niu, F., Kawakatsu, H., and Fukao, Y. (2003) Seismic evidence for a chemical heterogeneity in
472 the midmantle: A strong and slightly dipping seismic reflector beneath the Mariana
473 subduction zone. Journal of Geophysical Research: Solid Earth, 108, 1–12.

474 Ono, S., Suto, T., Hirose, K., Kuwayama, Y., Komabayashi, T., and Kikegawa, T. (2002)
475 Equation of state of Al-bearing stishovite to 40 GPa at 300 K. American Mineralogist, 87,
476 1486–1489.

477 Pawley, A.R., McMillan, P.F., and Holloway, J.R. (1993) Hydrogen in stishovite, with
478 implications for mantle water content. Science, 261, 1024–1026.

479 Petrícek, V., Dušek, M., and Palatinus, L. (2014) Crystallographic computing system JANA2006:
480 General features. Zeitschrift fur Kristallographie, 229, 345–352.

481 Range, K.-J., Rau, F., Klement, U., and Heyns, A.M. (1987) β-PtO2: high pressure synthesis of
482 single crystals and structure refinement. Materials Research Bulletin, 22, 1541–1547.

483 Renner, B., and Lehmann, G. (1986) Correlation of angular and bond length distortions in TO4

484 units in crystals. Zeitschrift fur Kristallographie - New Crystal Structures, 175, 43–59.

485 Rigaku, O.D. (2015) Crysalis Pro. Rigaku Oxford Diffraction Ltd, Yarnton, Oxfordshire,
486 England.

487 Robinson, K., Gibbs, G. V., and Ribbe, P.H. (1971) Quadratic Elongation: A Quantitative
488 Measure of Distortion in Coordination Polyhedra. Science, 172, 567–570.

489 Salje, E. (1993) Phase transitions in ferroelastic and co-elastic crystals. Cambridge University
490 Press.

491 Shannon, B.Y.R.D., H, M., Baur, N.H., Gibbs, O.H., Eu, M., and Cu, V. (1976) Revised
492 Effective Ionic Radii and Systematic Studies of Interatomie Distances in Halides and
493 Chaleogenides Central Research and Development Department , Experimental Station , E .
494 L Du Pont de Nemours The effective ionic radii of Shannon & Prewitt [Acta. Acta
495 Crystallographica Section A: Foundations of Crystallography, A 32, 751–767.

496 Simmons, N.A., and Gurrola, H. (2000) Multiple seismic discontinuities near the base of the
497 transition zone in the Earth's mantle. Nature, 405, 559–562.

498 Smyth, J.R., Swope, R.J., and Pawley, A.R. (1995) H in rutile-type compounds: II. Crystal
499 chemistry of Al substitution in H-bearing stishovite. American Mineralogist, 80, 454–456.

500 Spektor, K., Nylen, J., Stoyanov, E., Navrotsky, A., Hervig, R.L., Leinenweber, K., Holland,
501 G.P., and Häussermann, U. (2011) Ultrahydrous stishovite from high-pressure hydrothermal
502 treatment of SiO2. Proceedings of the National Academy of Sciences of the United States of
503 America, 108, 20918–20922.

504 Tauzin, B., Van Der Hilst, R.D., Wittlinger, G., and Ricard, Y. (2013) Multiple transition zone

505 seismic discontinuities and low velocity layers below western United States. Journal of
506 Geophysical Research: Solid Earth, 118, 2307–2322.

507 Tsutsumi, Y., Sakamoto, N., Hirose, K., Tagawa, S., Umemoto, K., Ohishi, Y., and Yurimoto, H.
508 (2024) Retention of water in subducted slabs under core–mantle boundary conditions.
509 Nature Geoscience, 17, 697–704.

510 Umemoto, K., Kawamura, K., Hirose, K., and Wentzcovitch, R.M. (2016) Post-stishovite
511 transition in hydrous aluminous SiO2. Physics of the Earth and Planetary Interiors, 255, 18–
512 26.

513 Wang, B., Buchen, J., Méndez, A.S.J., Kurnosov, A., Criniti, G., Liermann, H.P., and Marquardt,
514 H. (2023) Strong Effect of Stress on the Seismic Signature of the Post-Stishovite Phase
515 Transition in the Earth's Lower Mantle. Geophysical Research Letters, 50, 1–9.

516 Zhang, Y., Fu, S., Wang, B., and Lin, J.F. (2021) Elasticity of a Pseudoproper Ferroelastic
517 Transition from Stishovite to Post-Stishovite at High Pressure. Physical Review Letters, 126,
518 25701.

519 Zhang, Y., Fu, S., Karato, S. ichiro, Okuchi, T., Chariton, S., Prakapenka, V.B., and Lin, J.F.
520 (2022) Elasticity of Hydrated Al-Bearing Stishovite and Post-Stishovite: Implications for
521 Understanding Regional Seismic VS Anomalies Along Subducting Slabs in the Lower
522 Mantle. Journal of Geophysical Research: Solid Earth, 127, 1–16.

523 Zhang, Y., Chariton, S., He, J., Fu, S., Prakapenka, V.B., and Lin, J.F. (2023) Atomistic insight
524 into the ferroelastic post-stishovite transition by high-pressure single-crystal X-ray
525 diffraction refinements. American Mineralogist, 108, 110–119.

526

527 **FIGURE 1.** Representative unwarped images and full width at half maximum (FWHM) of 110
528 diffraction peaks of Al-bearing stishovite and post-stishovite at high pressure. Panels (a)-(d)
529 correspond to Al1.3-SiO_2, while panels (e)-(h) correspond to Al2.1-SiO_2. (a) and (b) are
530 unwarped images of the *hk*1 reciprocal planes of the Al1.3-SiO_2 crystal at 5.8 GPa and 38.0 GPa,
531 respectively. (e) and (f) are unwarped images of the *hk*2 reciprocal planes of the Al2.1-SiO_2
532 crystal at 6.5 GPa and 28.5 GPa, respectively. The white lines indicate reciprocal lattice grids
533 with *hkl* indices labeled on the left side and the bottom of the images. (c) and (g) show the 110
534 peaks integrated in azimuthal angle (χ) for the Al1.3-SiO_2 and Al2.1-SiO_2 crystal, respectively.
535 (d) and (h) show the 110 peaks integrated in diffraction angle (2θ) for the Al1.3-SiO_2 and Al2.1-
536 SiO_2 crystal, respectively. Black and red patterns in (c), (d), (g), and (h) show the 110 peaks in
537 stishovite and post-stishovite at high pressure, respectively. The FWHM and pressure values are
538 labeled next to each peak in the same color as the corresponding pattern.

539

540 **FIGURE 2.** Representative refined crystal structures of Al-bearing stishovite and post-stishovite
541 at high pressure. (a) Al1.3-SiO_2 in the stishovite phase with the space group of $P4_2/mnm$ (No.
542 136) at 7.1 GPa; (b) Al2.1-SiO_2 in the post-stishovite phase with the space group of *Pnnm* (No.
543 58) at 28.5 GPa. Obtained lattice parameters, oxygen coordinates, SiAl-O bond lengths, and O-
544 SiAl-O bond angles are labelled in the structures in (a) and (b).

545

546 **FIGURE 3.** Atomistic parameters of Al-bearing stishovite and post-stishovite at high pressure.
547 (a) Oxygen coordinates O*x* and O*y*; (b) mean bond lengths of equatorial (Si,Al)-O1(2) and apical

548 (Si,Al)-O3 bond; (c) mean bond angles of ∠(Si,Al)-O3-(Si,Al), ∠O1-(Si,Al)-O1, and ∠O1-
549 (Si,Al)-O3. The labels for atomic bonds and positions can be referred to Fig. 2. Lines are the best
550 fits using a linear or polynomial equation in (a) and (c) and a linear equation of state (Angel
551 2000; Gonzalez-Platas et al. 2016) in (b). Literature data are plotted for comparison (Smyth et al.
552 1995; Criniti et al. 2023; Zhang et al. 2023). Vertical blue and red lines show stishovite-to-post-
553 stishovite transition pressures of Al1.3-SiO_2 and Al2.1-SiO_2 at 21.1 GPa and 16.1 GPa,
554 respectively.

555

556 **FIGURE 4.** Al effects on the atomistic parameters of stishovite and their pressure dependence at
557 ambient conditions. (a) Oxygen coordinates; (b) pressure derivative of oxygen coordinates; (c)
558 (Si,Al)-O bond length; (d) linear modulus of (Si,Al)-O bond length; (e) bond angles; (f) pressure
559 derivative of bond angles. Lines in (a), (c), and (e) are the best linear fits to the data, while lines
560 in (b), (d), and (f) are connected between data points to guide the eye. Literature data are also
561 plotted for comparison (Smyth et al. 1995; Criniti et al. 2023; Zhang et al. 2023).

562

563 **FIGURE 5.** (Si,Al)O_6 octahedron parameters of Al-bearing stishovite and post-stishovite at high
564 pressure. (a) Octahedral volume (V_{oct}); (b) distortion index (D); (c) bond angle variance (σ^2).
565 Lines represent the best linear equation-of-state fits in (a) and the best linear or polynomial fits to
566 the data in (b) and (c). Data from previous reports are also plotted for comparison (Smyth et al.
567 1995; Criniti et al. 2023; Zhang et al. 2023). Vertical lines show the transition pressures of our
568 crystals with the same colors used in Fig. 3.

569

570 **FIGURE 6.** Al effects on the (Si,Al)O_6 octahedron parameters of stishovite and their pressure
571 dependence at ambient conditions. (a) octahedral volume (V_{oct}) and (b) bulk modulus (K_{oct}); (c)
572 distortion index (D) and (d) its first-order pressure derivative (dD/dP); (e) bond angle variance
573 (σ^2) and (f) its first-order pressure derivative ($d\sigma^2/dP$). Lines represent the best linear or
574 polynomial fits to the data in (a), (c), (d), and (e), while lines in (b) and (f) are connected
575 between data points to guide the eye. Literature data are also plotted for comparison (Smyth et al.
576 1995; Criniti et al. 2023; Zhang et al. 2023).

577

578 **FIGURE 7.** The transition pressure as a function of the (Al+H)/Si ratio where the Al, H, and Si
579 contents are in apfu. With the fixed transition pressure of pure-endmember stishovite, the best
580 linear fits (two black lines) were applied to hydrous SiO_2 samples with the SiO_2-H_2O mechanism
581 (Nisr et al. 2017; Zhang et al. 2021, 2023) and to Al(,H)-bearing samples with the SiO_2-AlOOH-
582 $AlO_{1.5}$ substitution mechanism from this study and literature reports (Lakshtanov et al. 2007b;
583 Bolfan-Casanova et al. 2009; Zhang et al. 2021, 2023; Ishii et al. 2022; Criniti et al. 2023). The
584 gray area along the lines shows a 95% confidence interval. The slopes of the lines, which
585 represent the rate of the transition pressure reduction, are labeled next to each line in the unit of
586 GPa.

587

588 **FIGURE 8.** Correlations between Landau parameters and the (Si,Al)O_6 octahedron rotation
589 angle (Φ) in Al-bearing post-stishovite. (a) Symmetry-bearing spontaneous strain (e_1 - e_2) as a
590 function of Φ. The e_1 - e_2 values are calculated using a formula of $(a-b)/\sqrt{a \times b}$, where a and
591 b are the axial lengths of the unit cell of the post-stishovite phase. Solid lines are the best linear

fits to the data. (b) Order parameter (Q) and (c) excess Landau free energy (ΔE). The Q and ΔE values were taken from previous Landau modeling results (Zhang et al. 2022). Solid lines show co-plotting of the Landau results and our polynomial fit results for Φ in Figure S3. The dashed lines in three panels represent the Landau parameters-Φ relationship in pure-endmember SiO_2 where the Landau parameters were taken from Zhang et al. (2021) and Φ was taken from Zhang et al. (2023).

FIGURE 9. Elastic properties of Al-bearing stishovite and post-stishovite as a function of the distortion index (D) of the (Si,Al)O_6 octahedron. (a) Elastic coefficients C_{11}, C_{12}, C_{22}, and C_{33}; (b) elastic coefficients C_{13}, C_{23}, C_{33}, C_{44}, C_{55}, and C_{66}; (c) adiabatic bulk modulus (K_S) and shear modulus (G); (d) compressional wave velocity (V_P) and shear wave velocity (V_S). The D values for Al1.3-SiO_2 and Al2.1-SiO_2 were taken from this study while that for pure-endmember SiO_2 was taken from Zhang et al. (2023). A typical error bar of D is shown in (d). Elasticity data for Al1.3-SiO_2 and Al2.1-SiO_2 were taken from Zhang et al. (2022) while that for pure-endmember SiO_2 was taken from Zhang et al. (2021). Vertical blue and red dashed lines show the phase transition from stishovite to post-stishovite in Al1.3-SiO_2 and Al2.1-SiO_2, respectively. The insert in (c) shows the Al substitution effect on the distortion of the (Si,Al)O_6 octahedron in the stishovite phase under pressure. The apical (Si,Al)-O3 bond is more compressible (longer blue arrows) than the equatorial (Si,Al)-O1(2) bond (shorter blue arrows). The Al substitution can lead to a less distorted (Si,Al)O_6 octahedron (yellow area with dashed-line border) than the pure SiO_6 octahedron (gray area with solid-line border).

This is the peer-reviewed, final accepted version for American Mineralogist, published by the Mineralogical Society of America.
The published version is subject to change. Cite as Authors (Year) Title. American Mineralogist, in press.
DOI: https://doi.org/10.2138/am-2023-9257. http://www.minsocam.org/

613

TABLE 1. Octahedral parameters of Al-bearing stishovite and post-stishovite at high pressure

P (GPa)	V_{oct} (Å)	D	σ^2 (deg^2)	Φ (°)
		Al1.3-SiO_2		
0.0001	7.451(7)	0.01300(1)	26.83(3)	0
2.5(0)	7.387(7)	0.01256(1)	26.92(3)	0
5.1(0)	7.332(10)	0.01060(1)	26.50(3)	0
5.8(0)	7.321(12)	0.00976(2)	26.10(4)	0
7.1(1)	7.289(14)	0.00886(2)	25.80(5)	0
9.4(3)	7.247(12)	0.00701(1)	25.25(4)	0
12.4(0)	7.176(9)	0.00866(1)	27.10(4)	0
17.2(2)	7.076(12)	0.00774(1)	27.85(5)	0
19.4(2)	7.051(7)	0.00563(1)	26.62(3)	0
20.4(1)	7.022(7)	0.00598(1)	26.66(3)	0
21.0(1)	6.994(9)	0.00598(1)	27.17(4)	0
26.3(3)	6.899(18)	0.00683(2)	27.86(7)	0.9(2)
28.1(3)	6.861(21)	0.00783(2)	28.91(9)	1.5(2)
29.5(0)	6.847(10)	0.00077(0)	24.78(4)	1.4(1)
34.4(2)	6.770(9)	0.00127(0)	25.85(3)	2.1(1)
38.0(3)	6.703(12)	0.00689(1)	29.90(5)	2.2(1)
		Al2.1-SiO_2		
0.0001	7.499(12)	0.01363(2)	26.48(4)	0
1.3(0)	7.456(7)	0.01259(1)	26.35(3)	0
3.0(0)	7.437(7)	0.01122(1)	25.66(3)	0
5.1(0)	7.395(10)	0.01067(1)	26.41(3)	0
6.5(1)	7.370(5)	0.00853(1)	25.23(2)	0
9.2(1)	7.293(7)	0.00788(1)	25.59(3)	0
11.0(2)	7.262(7)	0.00774(1)	25.79(3)	0
13.5(2)	7.236(10)	0.00589(1)	24.75(3)	0
14.6(2)	7.200(9)	0.00689(1)	25.92(3)	0
22.0(1)	7.086(11)	0.00092(0)	23.05(3)	1.3(1)
24.0(1)	6.987(19)	0.01019(3)	30.25(8)	1.4(2)
25.9(1)	7.001(16)	0.00332(1)	26.28(6)	1.7(2)
28.5(1)	6.943(17)	0.00614(2)	28.64(7)	2.1(2)

614

615

616

617

This is the peer-reviewed, final accepted version for American Mineralogist, published by the Mineralogical Society of America.
The published version is subject to change. Cite as Authors (Year) Title. American Mineralogist, in press.
DOI: https://doi.org/10.2138/am-2023-9257. http://www.minsocam.org/

618

TABLE 2. Linear EoS parameters of (Si,Al)-O bond lengths and EoS parameters of the (Si,Al)O_6 octahedron (* fixed value)

Crystal	Al1.3-SiO_2	Al2.1-SiO_2	Al1.7-SiO_2	SiO_2
Reference	This study	This study	Criniti et al. (2023)	Zhang et al. (2023)
			apical (Si,Al)-O3	
l_0	1.8162(13)	1.8220(30)	1.8154(15)	1.8075(6)
$K_{0,l}$	556(9)	478(13)	680(47)	618(12)
$K_{0,l}$'	12*	12*	12*	12*
			equatorial (Si,Al)-O1(2)	
l_0	1.7641(9)	1.7669(14)	1.7664(8)	1.7565(4)
$K_{0,l}$	1287(35)	1807(121)	1135(64)	1453(49)
$K_{0,l}$'	12*	12*	12*	12*
			(Si,Al)O_6 octahedron	
$V_{0,oct}$	7.4514(19)	7.4991(19)	7.4653(19)	7.3506(5)
$K_{0,oct}$	304.6(26)	333.1(83)	313.8(31)	368.0(103)
$K_{0,oct}$'	4*	4*	4*	4*

619

620

621

622

623

624

625

626

This is the peer-reviewed, final accepted version for American Mineralogist, published by the Mineralogical Society of America.
The published version is subject to change. Cite as Authors (Year) Title. American Mineralogist, in press.
DOI: https://doi.org/10.2138/am-2023-9257. http://www.minsocam.org/

627 **Fig. 1**

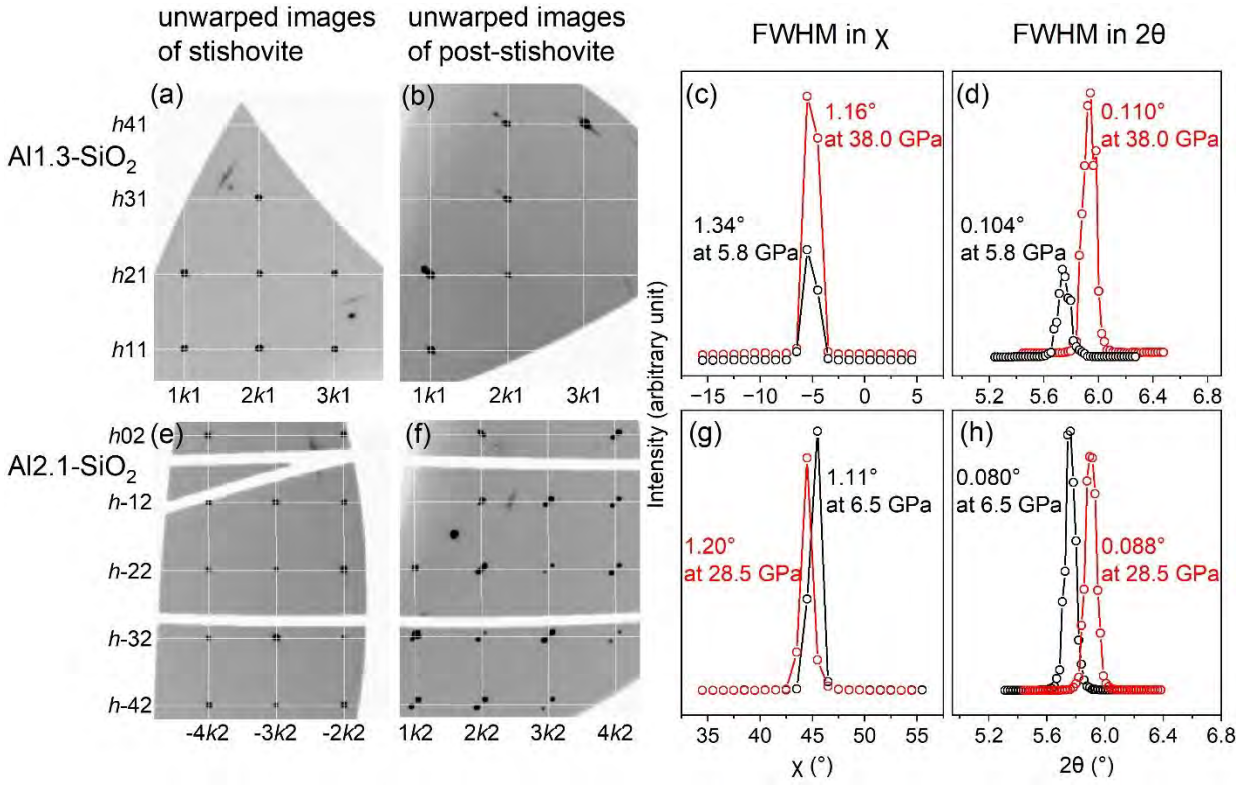

628

629

630

631

632

633

634

635

636

This is the peer-reviewed, final accepted version for American Mineralogist, published by the Mineralogical Society of America.
The published version is subject to change. Cite as Authors (Year) Title. American Mineralogist, in press.
DOI: https://doi.org/10.2138/am-2023-9257. http://www.minsocam.org/

637 **Fig. 2**

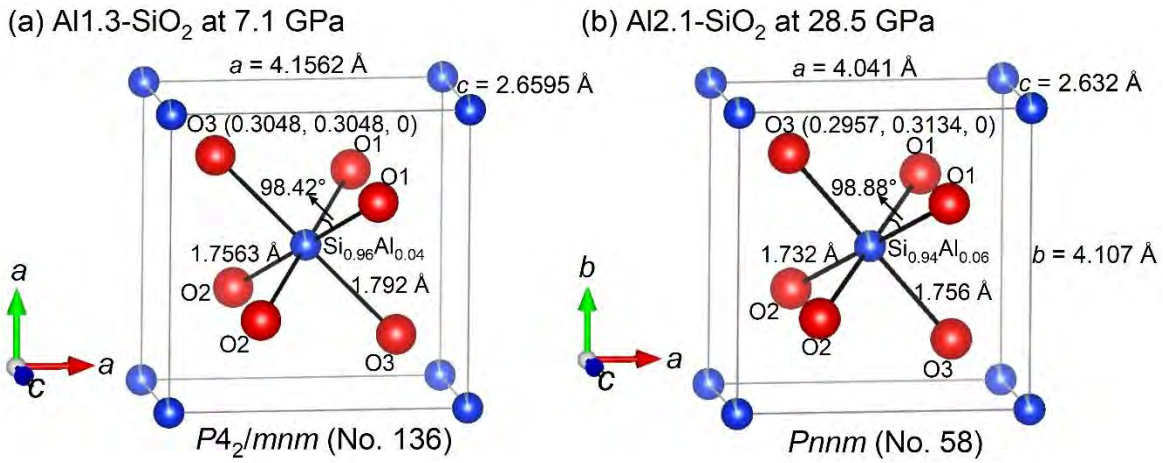

638

639

640

641

642

643

644

645

646

647

648

649

650

This is the peer-reviewed, final accepted version for American Mineralogist, published by the Mineralogical Society of America.
The published version is subject to change. Cite as Authors (Year) Title. American Mineralogist, in press.
DOI: https://doi.org/10.2138/am-2023-9257. http://www.minsocam.org/

651 **Fig. 3**

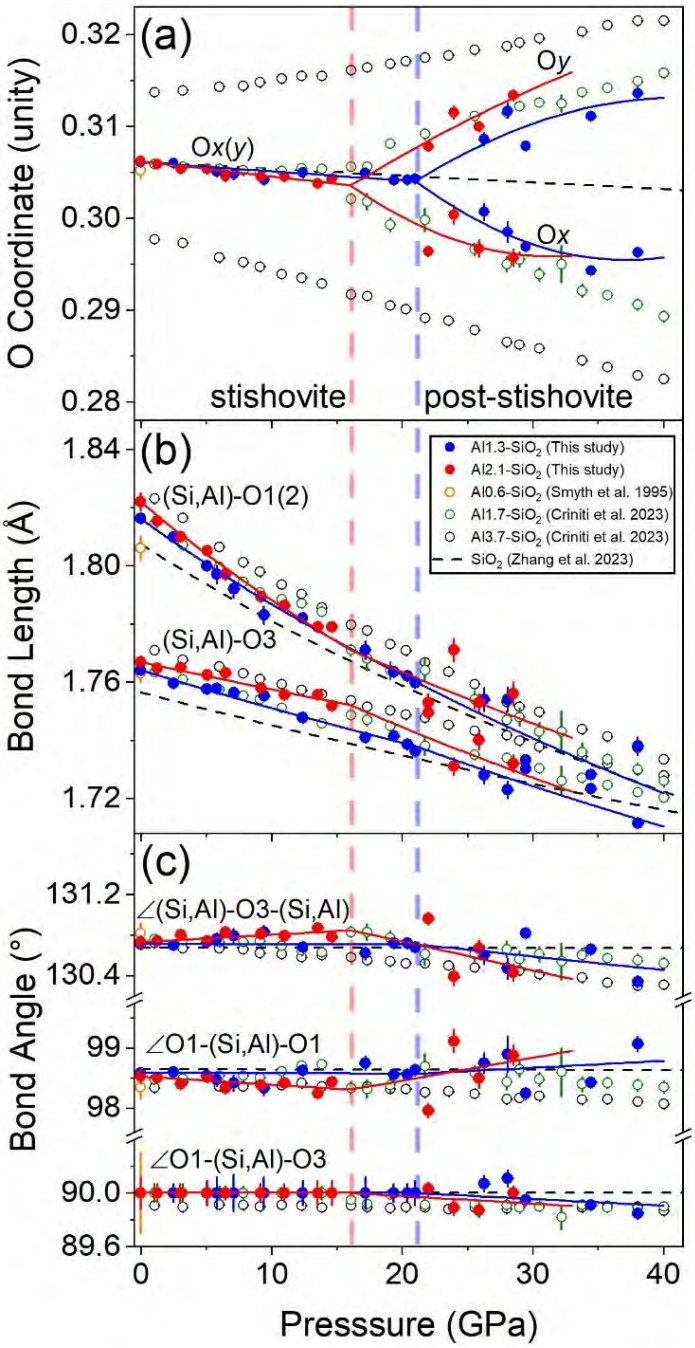

652

653

654

655

This is the peer-reviewed, final accepted version for American Mineralogist, published by the Mineralogical Society of America.
The published version is subject to change. Cite as Authors (Year) Title. American Mineralogist, in press.
DOI: https://doi.org/10.2138/am-2023-9257. http://www.minsocam.org/

Fig. 4

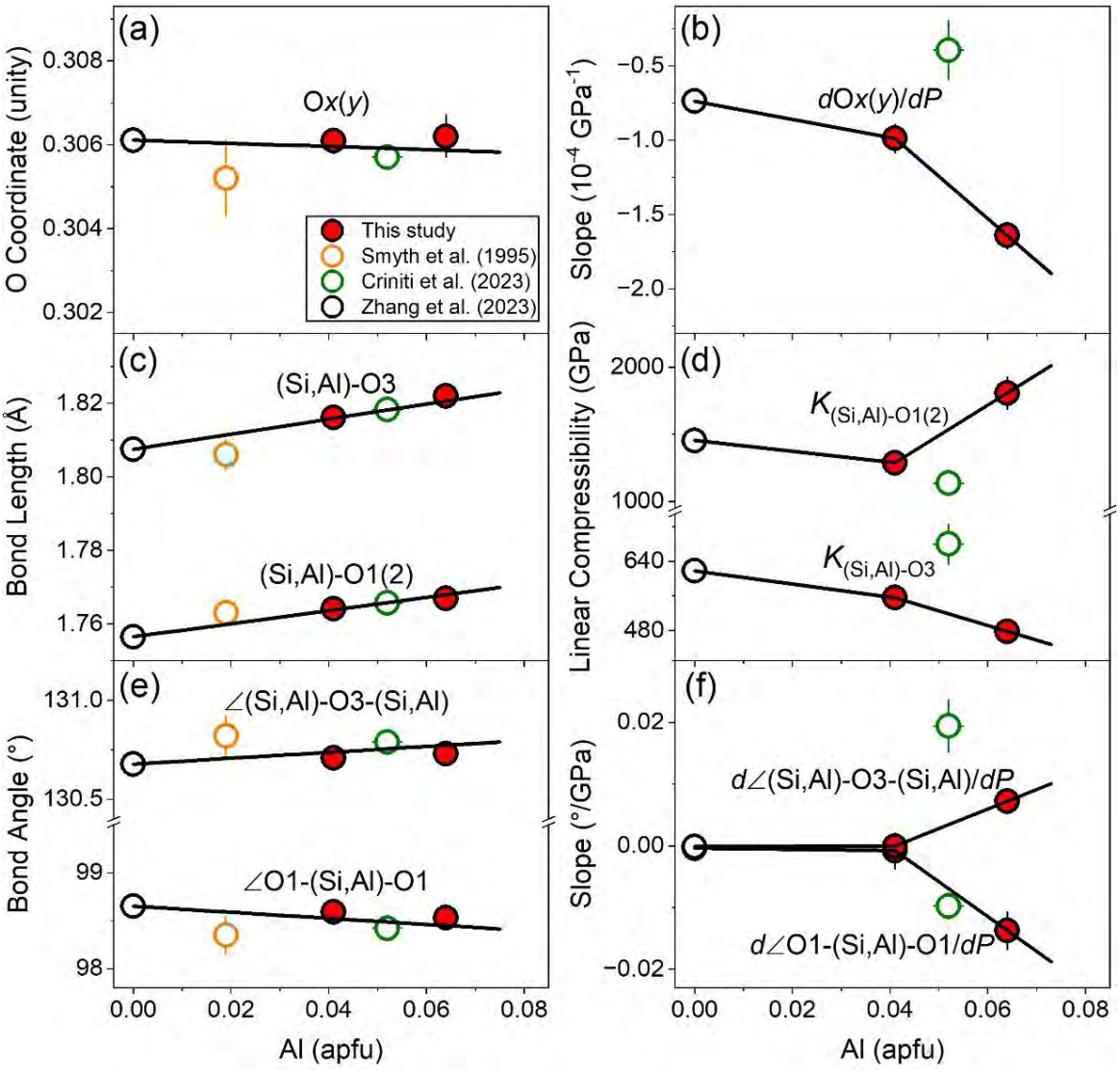

This is the peer-reviewed, final accepted version for American Mineralogist, published by the Mineralogical Society of America.
The published version is subject to change. Cite as Authors (Year) Title. American Mineralogist, in press.
DOI: https://doi.org/10.2138/am-2023-9257. http://www.minsocam.org/

663 **Fig. 5**

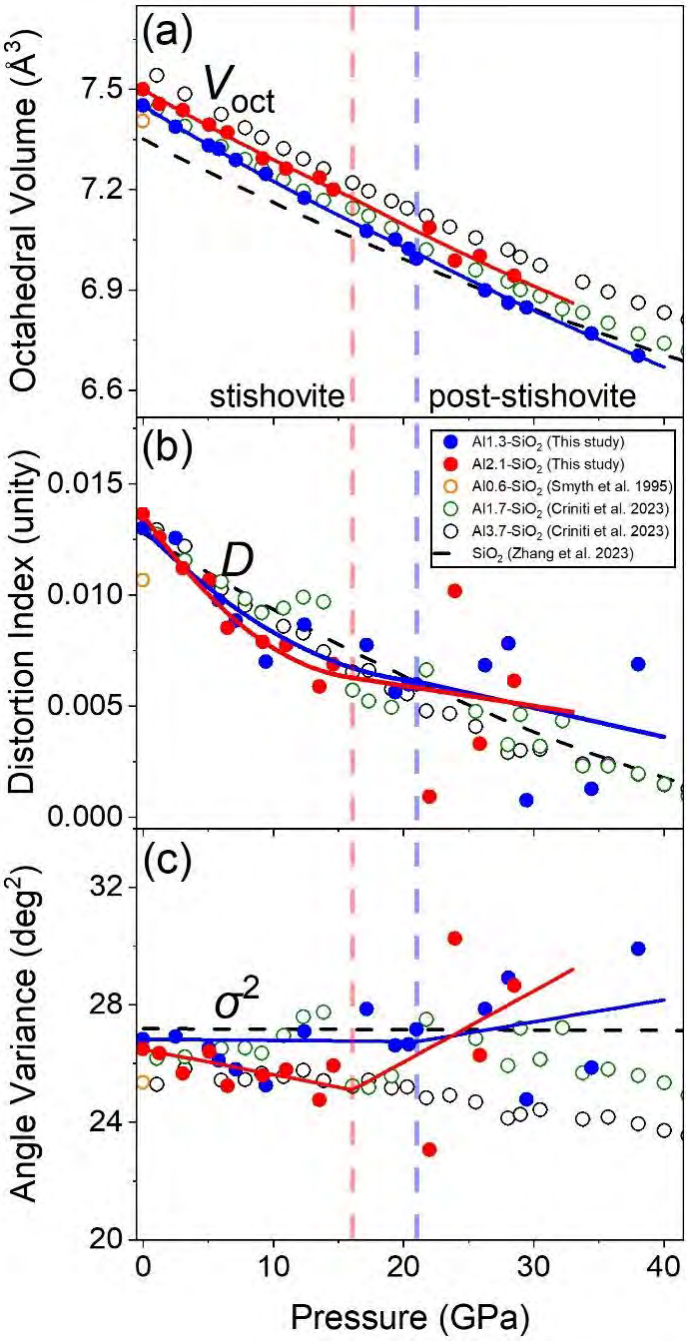

664

665

666

667

This is the peer-reviewed, final accepted version for American Mineralogist, published by the Mineralogical Society of America.
The published version is subject to change. Cite as Authors (Year) Title. American Mineralogist, in press.
DOI: https://doi.org/10.2138/am-2023-9257. http://www.minsocam.org/

668 **Fig. 6**

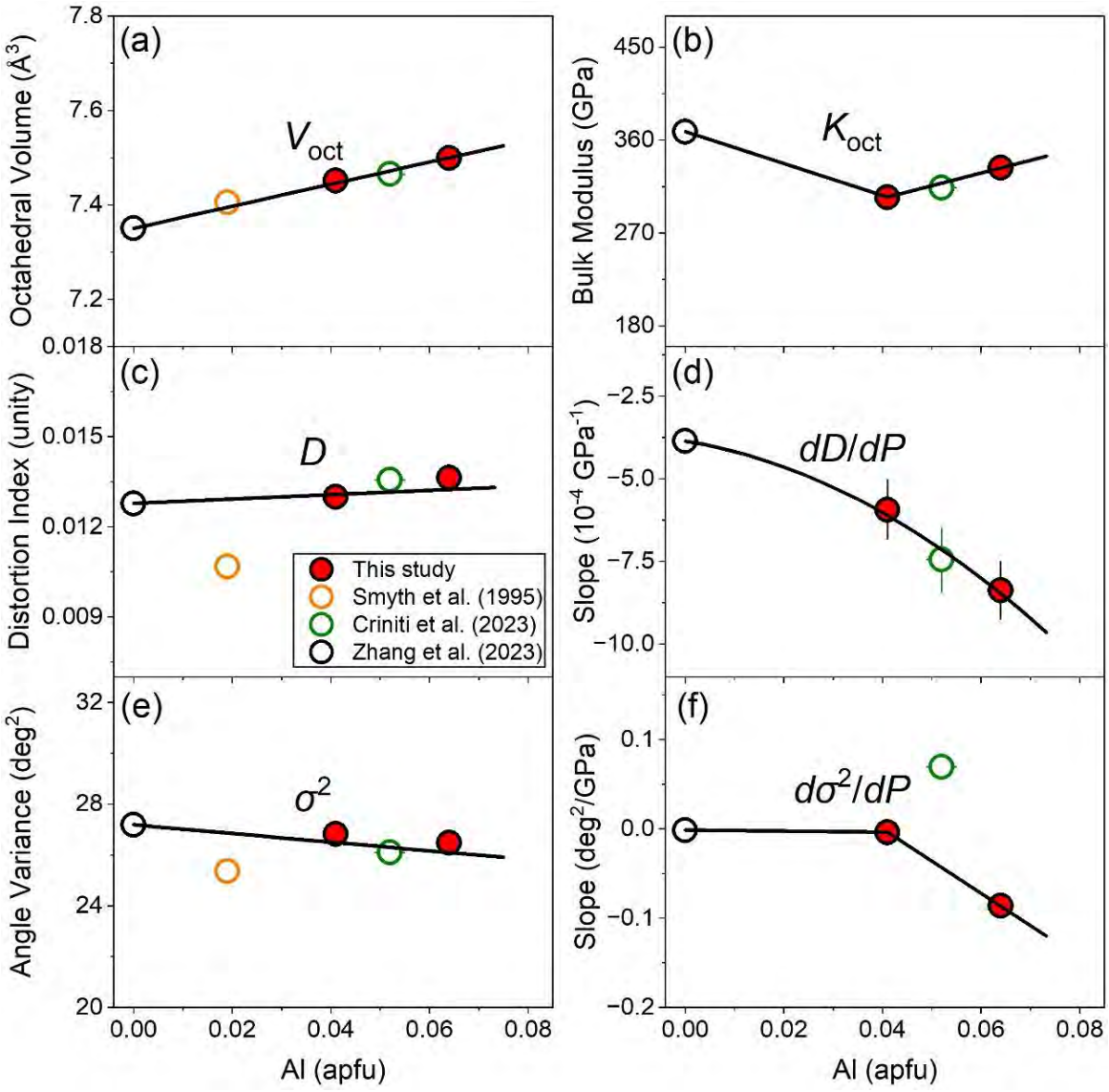

669

670

671

672

673

674

This is the peer-reviewed, final accepted version for American Mineralogist, published by the Mineralogical Society of America.
The published version is subject to change. Cite as Authors (Year) Title. American Mineralogist, in press.
DOI: https://doi.org/10.2138/am-2023-9257. http://www.minsocam.org/

675 **Fig. 7**

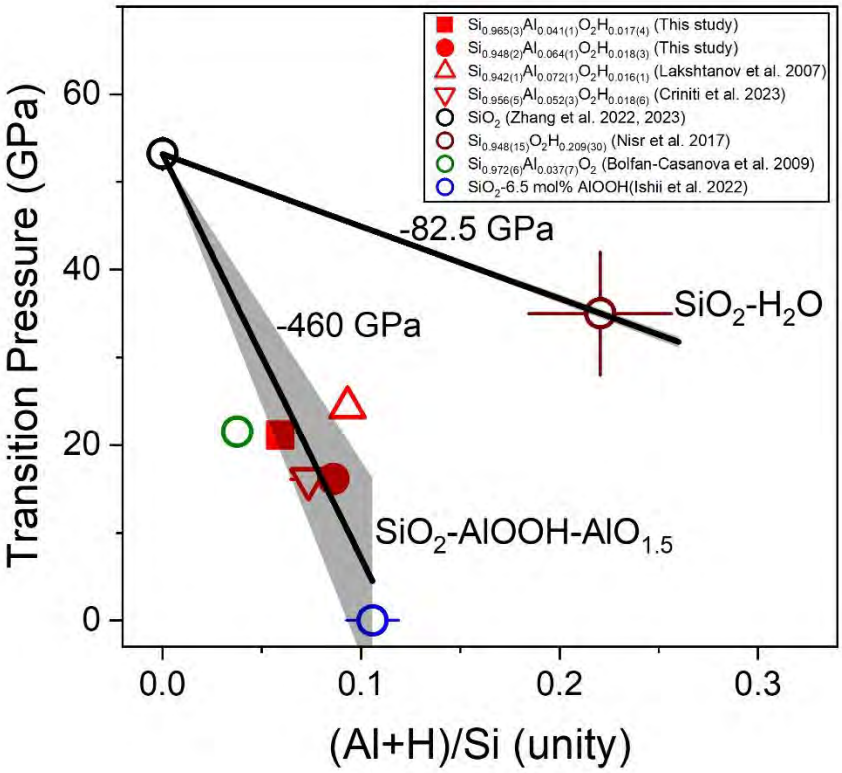

676

677

678

679

680

681

682

683

684

This is the peer-reviewed, final accepted version for American Mineralogist, published by the Mineralogical Society of America.
The published version is subject to change. Cite as Authors (Year) Title. American Mineralogist, in press.
DOI: https://doi.org/10.2138/am-2023-9257. http://www.minsocam.org/

685 **Fig. 8**

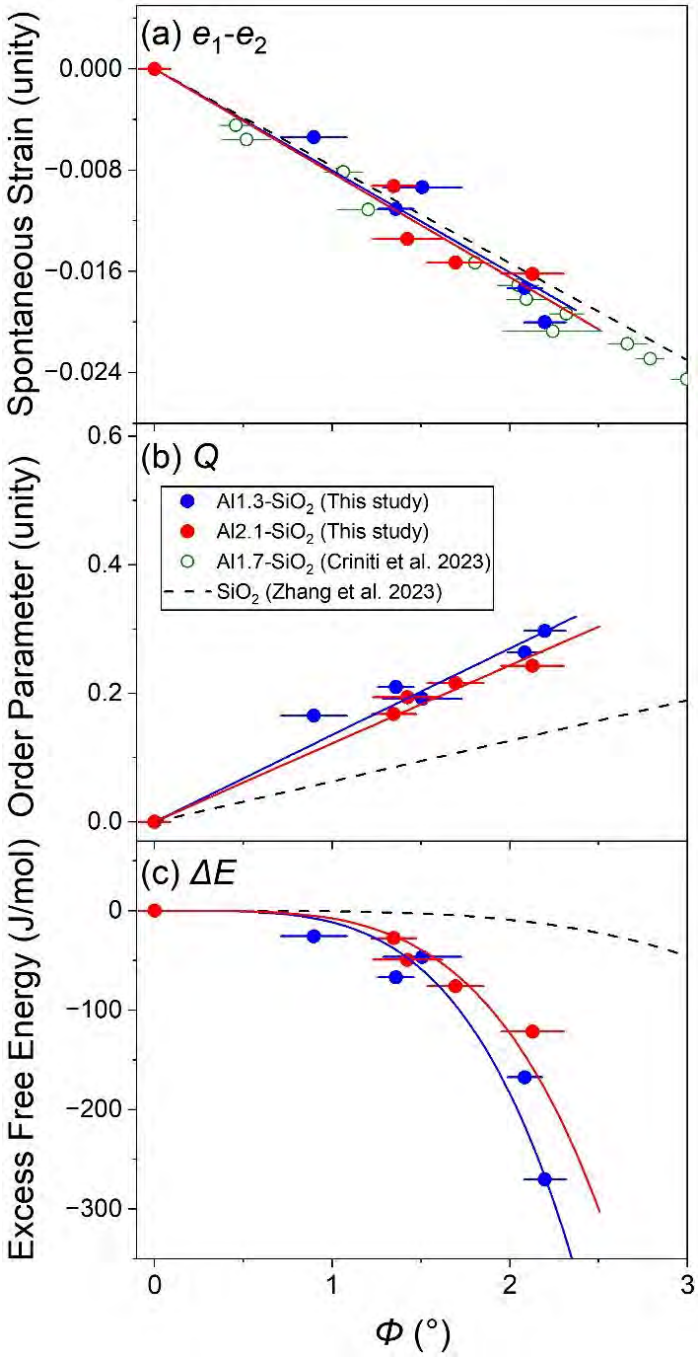

686

687

688

This is the peer-reviewed, final accepted version for American Mineralogist, published by the Mineralogical Society of America.
The published version is subject to change. Cite as Authors (Year) Title. American Mineralogist, in press.
DOI: https://doi.org/10.2138/am-2023-9257. http://www.minsocam.org/

689 **Fig. 9**

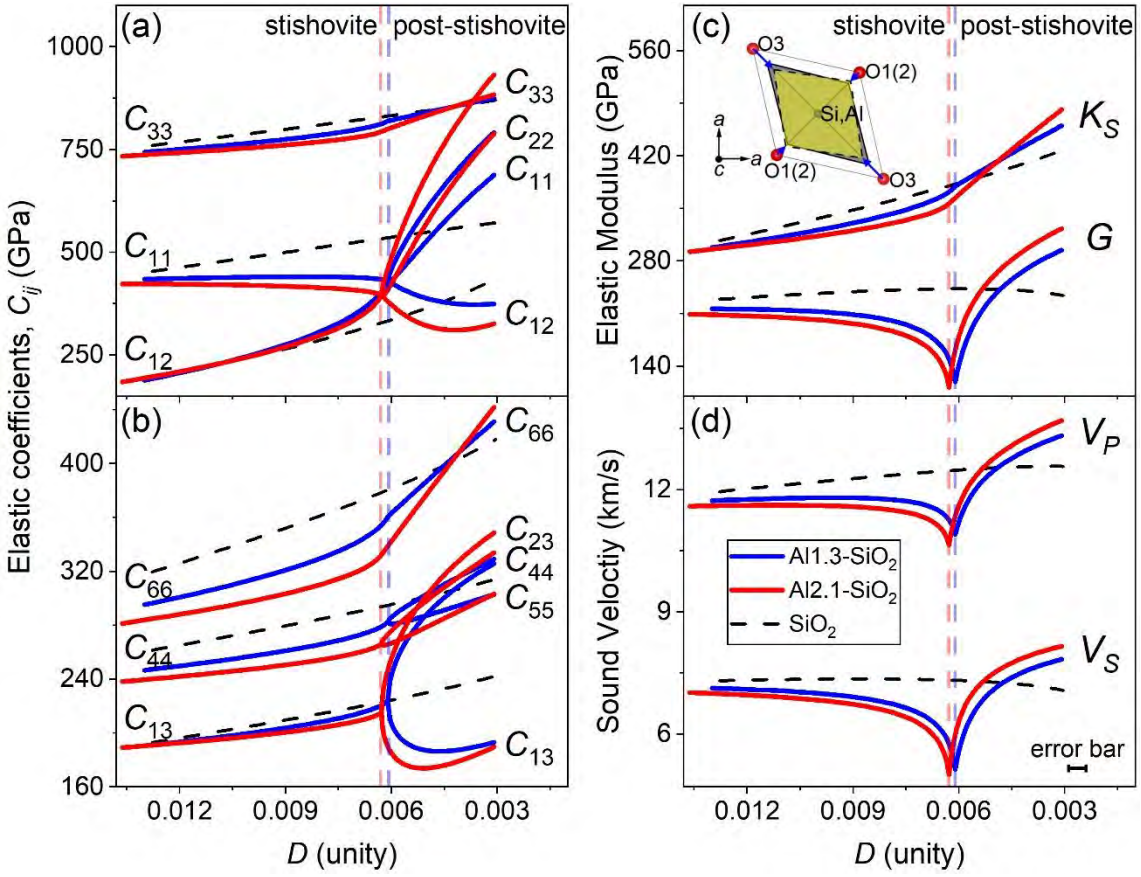

690

691

692

693

694